Superresolution microscopy of the β-carboxysome reveals a homogeneous matrix

Matthew J. Niederhuber[a,b,†], Talley J. Lambert[c], Clarence Yapp[d], Pamela A. Silver[a,b], and Jessica K. Polka[a,b,*]

[a]Department of Systems Biology, [c]Department of Cell Biology, and [d]Image and Data Analysis Core, Harvard Medical School, Boston, MA 02115; [b]Wyss Institute for Biologically Inspired Engineering, Harvard University, Boston, MA 02115

ABSTRACT Carbon fixation in cyanobacteria makes a major contribution to the global carbon cycle. The cyanobacterial carboxysome is a proteinaceous microcompartment that protects and concentrates the carbon-fixing enzyme ribulose-1,5-bisphosphate carboxylase/oxygenase (RuBisCO) in a paracrystalline lattice, making it possible for these organisms to fix CO_2 from the atmosphere. The protein responsible for the organization of this lattice in beta-type carboxysomes of the freshwater cyanobacterium *Synechococcus elongatus*, CcmM, occurs in two isoforms thought to localize differentially within the carboxysome matrix. Here we use wide-field time-lapse and three-dimensional structured illumination microscopy (3D-SIM) to study the recruitment and localization of these two isoforms. We demonstrate that this superresolution technique is capable of distinguishing the localizations of the outer protein shell of the carboxysome and its internal cargo. We develop an automated analysis pipeline to analyze and quantify 3D-SIM images and generate a population-level description of the carboxysome shell protein, RuBisCO, and CcmM isoform localization. We find that both CcmM isoforms have similar spatial and temporal localization, prompting a revised model of the internal arrangement of the β-carboxysome.

INTRODUCTION

RuBisCO (ribulose-1,5-bisphosphate carboxylase/oxygenase), the primary enzyme of carbon fixation, is ubiquitous in autotrophic organisms. However, it is notoriously inefficient and readily participates in energetically wasteful side reactions with O_2 (Andersson and Backlund, 2008). Many organisms that rely on RuBisCO to acquire inorganic carbon tune the enzyme's local microenvironment to achieve sufficient levels of carbon fixation. While plants can do this within membrane barriers, many single-celled organisms have evolved a strategy of proteinaceous compartmentalization.

The carboxysome is a bacterial microcompartment found in cyanobacteria and prokaryotic chemoautotrophs. Composed of thousands of individual subunits, the carboxysome encapsulates RuBisCO and carbonic anhydrase (CA) within an icosahedral shell, making survival possible at atmospheric levels of CO_2 (Figure 1A; Badger and Price, 2003; Rae *et al.*, 2012, 2013; Kerfeld and Melnicki, 2016).

While evolutionarily distinct carboxysomes share many similar structural features, the RuBisCO in the beta-type carboxysome (β-carboxysome) of the freshwater cyanobacterium *Synechococcus elongatus* PCC7942 is organized into a paracrystalline lattice (Kaneko *et al.*, 2006; Rae *et al.*, 2013). The structural protein CcmM has been implicated in connecting individual RuBisCO enzymes into an ordered matrix, resulting in the observed dense crystalline packing (Long *et al.*, 2007, 2010; Cot *et al.*, 2008; Cameron *et al.*, 2013). The full-length 58-kDa CcmM protein of PCC7942 is characterized by an N-terminal CA binding domain and three repeating domains toward the C-terminal end that have sequence homology to the small subunit of RuBisCO (Figure 1B; Price *et al.*, 1993). Owing to an internal ribosomal entry site (IRES), CcmM is translated as two

isoforms, a full-length protein (M58) and a 35-kDa truncated version (M35) that consists of only the three small subunit-like (SSU-like) domains (Long et al., 2007, 2010).

The current model of β-carboxysome internal structure suggests that the SSU-like domains of CcmM displace some of the small subunits of the $RbcL_8RbcS_8$ RuBisCO holoenzyme and tether multiple enzymes together into a dense network (Figure 1C; Long et al., 2007, 2010; Rae et al., 2013; Kerfeld et al., 2016). Copurification and yeast two-hybrid experiments have shown that RuBisCO readily complexes with both isoforms of CcmM in PCC7942 (Long et al., 2007; Cot et al., 2008). In addition, fluorescence-tagging experiments have demonstrated that M35 alone is capable of nucleating an assembly of tagged RuBisCO if at least two of the SSU-like domains are present. However, M35 is not sufficient to cause encapsulation by recruiting shell components in the absence of M58 (Cameron et al., 2013). Densitometry analyses of Western blot experiments have found imbalanced ratios of RbcS to RbcL (~5:8) in PCC7942 cell lysates, suggesting that some RbcS binding sites in the complex may instead be occupied by CcmM SSU-like domains (Long et al., 2011). These findings have supported a model of carboxysome architecture and stepwise assembly in which M35 nucleates a core of RuBisCO. In this model, M58 is limited to a layer beneath the shell where it can interact with CcmN, CA, and shell components. While this model predicts that the CcmM isoforms are differentially localized, these predictions have yet to be directly tested.

To test this model, we fluorescently tagged CcmM to visualize its assembly and the localization of CcmM isoforms in vivo. Previous work has shown that completely replacing CcmM with tagged

fusions does not disrupt carboxysome function (Long et al., 2007; Cameron et al., 2013). Loss of either isoform of CcmM produces cells that have a high CO_2 requirement (HCR) for growth (Woodger et al., 2005; Long et al., 2010). However, complementation of such mutants with tagged copies of CcmM has been shown to rescue this phenotype (Long et al., 2007; Cameron et al., 2013).

Here we show the successful complementation of a ΔccmM mutant with a dually fluorescently tagged integration of ccmM. This dual-tagging strategy does not significantly impair carboxysome formation, morphology, or function. In our time-lapse fluorescence microscopy data, we find that M58 may accumulate less rapidly than M35 during initial assembly but that the long isoform is present from the earliest points of detectable carboxysome assembly. Using superresolution three-dimensional structured illumination microscopy (3D-SIM), we examined the relative localization of carboxysome shell, CcmM, and RuBisCO proteins. Our 3D-SIM data do not support a model of carboxysome internal organization in which M58 is limited to a layer just beneath the external protein shell. These data support a revised model of carboxysome internal structure in which M35 and M58 isoforms are both integrated deep within the core of the carboxysome and are both involved with the early steps of carboxysome assembly.

RESULTS

Fluorescent fusions to CcmM complement a deletion of the wild-type gene

We constructed a fluorescently tagged copy of ccmM by fusing a blue fluorescent protein (mTagBFP2) to the N-terminus and a yellow-green fluorescent protein (mNeonGreen) to the C-terminus to make *mTagBFP2-ccmM-mNeonGreen* (*B-ccmM-N*). We subsequently integrated this construct, which is under the control of the isopropyl β-D-1-thiogalactopyranoside (IPTG) inducible promoter P*trc*, into the genome of an *S. elongatus* PCC7942 Δ*ccmM::HygR* mutant strain (Figure 2A), and verified expression by Western blot analysis (Figure 2B). This strategy allowed us to visually separate full-length M58 from truncated M35 by blue fluorescence. We found that P*trc* was sufficiently active to produce protein without induction. Consequently we never induced the Δ*ccmM* + *B-ccmM-N* strain, including for Western blot analysis, unless otherwise noted. We blotted lysates of wild-type (WT), Δ*ccmM*, and Δ*ccmM* + *B-ccmM-N* strains for the presence of CcmM (Figure 2B). In WT 7942 cells, we detected two bands at ~60 and ~40 kDa corresponding to the two native CcmM isoforms M58 and M35. In the Δ*ccmM* strain, these bands were absent. In the Δ*ccmM* + *B-ccmM-N* gene complement, we detected two bands at ~140 and ~70 kDa corresponding to expected molecular weight shifts of ~60 (both fluorescent tags) and ~30 kDa (mNeonGreen alone). The observed weight shift of the tagged CcmM demonstrates that the CcmM IRES is not impaired by the presence of N- and C-terminal tags
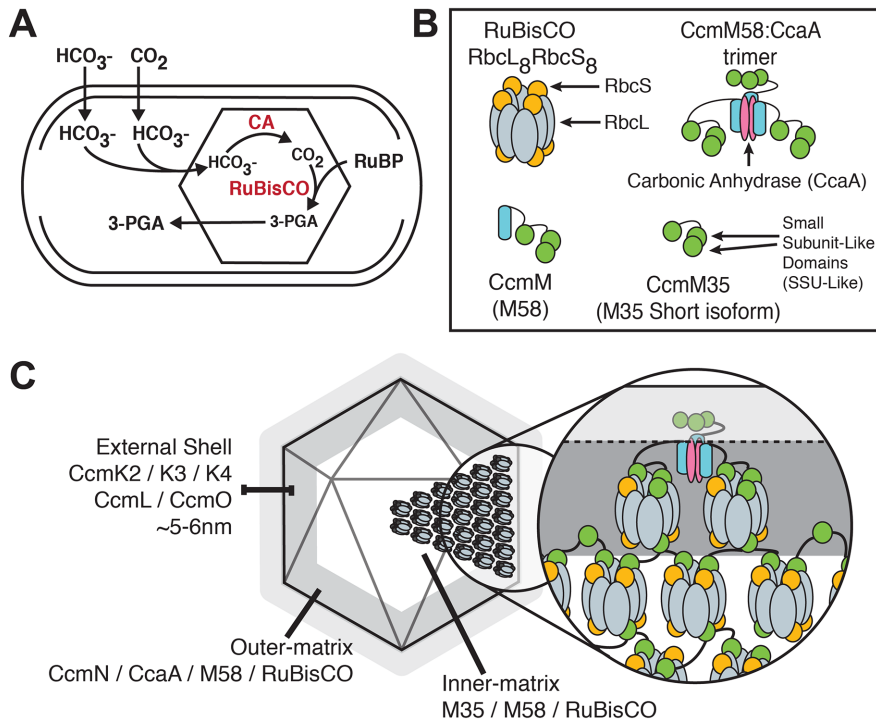
FIGURE 1: Current model of the cyanobacterial carboxysome internal structure. (A) *S. elongatus* uses the carboxysome to concentrate and protect its RuBisCO enzymes. Through a multistep process, bicarbonate passes into the carboxysome, is converted to CO_2 by CA, and is then fixed by RuBisCO to form 3-phosphoglyceric acid (3-PGA). (B) Legend of proteins and protein complexes of the carboxysome interior. (C) Illustration of current model of differential CcmM isoform localization and structural function within the carboxysome interior. Protein illustrations based on Rae et al. (2013).
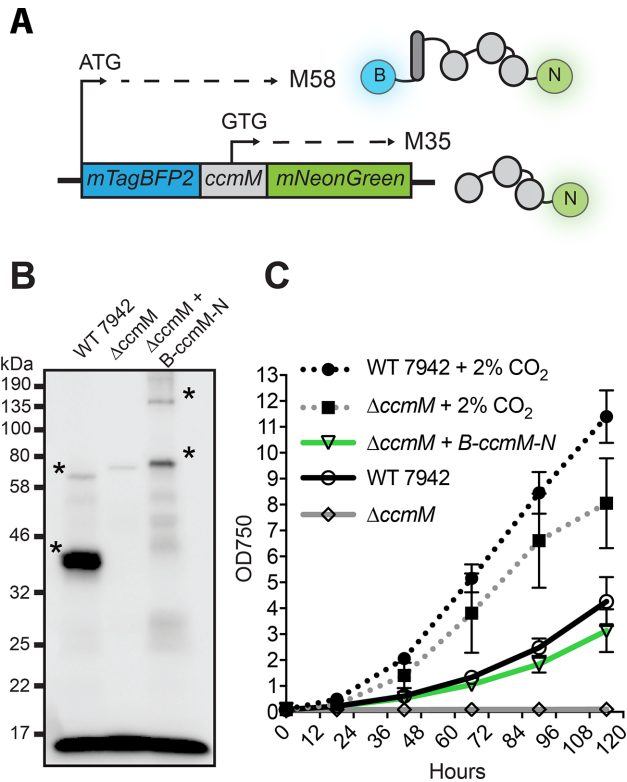
FIGURE 2: Fluorescently tagged *ccmM* integrated into the genome of a Δ*ccmM* knockout produces both CcmM isoforms and restores growth in atmospheric air conditions. (A) Diagram of fluorescently tagged *ccmM*. N- and C-terminal fusion of mTagBFP2 and mNeonGreen produces short and long isoforms with different fluorescence characteristics. This construct was integrated into a Δ*ccmM* background to yield the Δ*ccmM* + *mTagBFP2-ccmM-mNeonGreen* (*B-ccmM-N*) strain. (B) Anti-CcmM Western blot of WT, Δ*ccmM*, and *B-ccmM-N*. Full-length M58 isoform of CcmM is ~58 kDa, while the truncated M35 is ~35 kDa. The fluorescent fusions of mTagBFP2-M58-mNeonGreen and M35-mNeonGreen have expected molecular weights of ~113 and 63 kDa, respectively. (C) Growth curves of WT 7942 (*n* = 6 for atmospheric air, *n* = 5 for 2% CO₂), Δ*ccmM* (*n* = 6 for atmospheric air and 2% CO₂), and the *B-ccmM-N* genetic complement (*n* = 6 for atmospheric air and 2% CO₂). Dotted lines denote cultures grown with 2% supplemented CO₂. Solid lines denote cultures grown in atmospheric air conditions without CO₂ supplementation.

and that both long and short CcmM isoforms are translated. We also made a reciprocally tagged version of the CcmM complement (mNeonGreen-CcmM-mTagBFP2) but did not use it for further analysis, because Western blotting showed the presence of protein degradation (Supplemental Figure S1).

The dual-fusion *B-ccmM-N* transgene produced different relative abundances of each CcmM isoform compared with bands detected in WT (Figure 2B). A greater amount of the shorter M35 than full-length M58 isoform was detected in WT cells, matching expectations based on previously reported ratios (Long *et al.*, 2007). In cells expressing the dual-fusion *B-ccmM-N* transgene, we observed a reduction in M35 levels relative to M58, though M35 remained more abundant. A similar effect on isoform levels has been observed previously upon tagging CcmM (Long *et al.*, 2007, see *Discussion*). Thus carboxysomes formed with dual-tagged CcmM are inherently perturbed from WT in their protein composition.

Our tagged *ccmM* complement grew at a rate comparable to WT at atmospheric levels of CO₂ (Figure 2C). We grew WT 7942, the Δ*ccmM* mutant, and the Δ*ccmM* + *B-ccmM-N* complement in ambient air and 2% CO₂ conditions, measured optical density at 750 nm (OD₇₅₀), and calculated doubling times between the 0- and 18-h time points (see *Materials and Methods*). Approximate doubling times were calculated with these early time points to minimize potential impacts of self-shading. Both WT and Δ*ccmM* cells grew well when cultured with 2% CO₂ flowed through the incubator headspace, with doubling times of 7.7 ± 0.6 h (*n* = 5, error = SD) and 15.4 ± 9.2 h (*n* = 6, error = SD), respectively. As expected, Δ*ccmM* mutant growth was dependent on supplemented CO₂ (Long *et al.*, 2010); these cells showed no growth under conditions of atmospheric levels of CO₂. In contrast, the Δ*ccmM* + *B-ccmM-N* complement grew well in air with no supplemented CO₂, with a doubling time of 17.8 ± 2.3 h (*n* = 6, error = SD). This growth rate is similar to that of WT cells grown with atmospheric levels of CO₂, which had a doubling time of 14.1 ± 2.3 h (*n* = 6, error = SD), indicating that our engineered strain is capable of fixing carbon and that carboxysome function is not severely impaired by the dual-fusion *ccmM* complement. Because both the M58 and M35 isoforms of CcmM are required for growth without CO₂ supplementation (Long *et al.*, 2010), our data indicate that both isoforms produced by our dual fusion are functional.

Carboxysomes formed in the Δ*ccmM* + *B-ccmM-N* complement were structurally like those of WT cells. Using transmission electron microscopy (TEM), we imaged ultrathin sections of fixed cells from WT 7942, Δ*ccmM*, and Δ*ccmM* + *B-ccmM-N* strains (Figure 3). Carboxysomes in WT PCC7942 cells had an average maximum width of 179 ± 33 nm (*n* = 26, error = SD; Figure 3A). Carboxysomes in Δ*ccmM* + *B-ccmM-N* cells generally had a normal appearance and shape with visibly angled facets and often clear hexagonal geometry, but were noticeably larger, with an average maximum diameter of 319 ± 92 nm (*n* = 41, error = SD; Figure 3C). This is not unexpected; it has been previously reported that His-tagged *ccmM* complements increase carboxysome size (Long *et al.*, 2007). Measured carboxysome diameters in WT and Δ*ccmM* + *B-ccmM-N* cells were found to have notably different frequency distributions (Figure 3D). Importantly, the section thickness used for TEM is narrower (~70 nm) than the diameter of a typical carboxysome (~150–250 nm), meaning that measured diameters likely underestimate true size. We compared the distribution we observed in WT to that of a theoretical model that calculated diameter based on slices through a spherical object and found the frequency distribution (*n* = 40, mode = 150 nm) to be similar to that of WT (*n* = 26, mode = 200 nm; Figure 3D). Occasionally, dense masses at the cell poles were observed in Δ*ccmM* + *B-ccmM-N* micrographs, most likely indicating protein aggregation. Because we were using this strain without induction and no effective repressors exist, we cannot know whether reducing expression would prevent aggregate formation. However, IPTG-induced cells observed with 3D-SIM display a dramatic increase in polar protein aggregation, often filling a large portion of the cell, confirming that overexpression of this construct leads to aggregation (Supplemental Figure S2).

The two CcmM isoforms have similar dynamics during carboxysome assembly

The two CcmM isoforms M35 and M58 displayed similar dynamics during carboxysome biogenesis, though mTagBFP2 and mNeonGreen fluorophores differed in their rate of accumulation, particularly during early stages of assembly. Using wide-field fluorescence microscopy, we imaged the Δ*ccmM* complement (*B-ccmM-N*) at
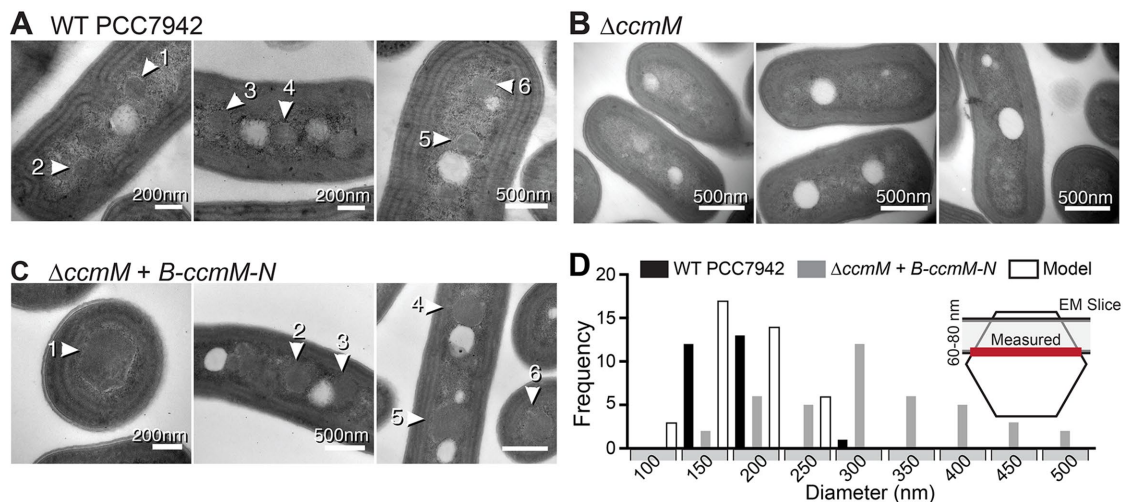
FIGURE 3: Transmission electron micrographs show the formation of carboxysomes in Δ*ccmM* cells complemented with fluorescently tagged *ccmM*. (A, 1–6) Carboxysomes (numbers and white arrows) in WT PCC7942 cells show characteristic hexagonal geometry. (B) Three micrographs of the Δ*ccmM* knockout show the absence of carboxysomes. (C, 1–6) Integration of the fluorescently tagged *B-ccmM-N* construct into the Δ*ccmM* knockout rescues the formation of apparently normal carboxysomes. Scale bar in right panel of C: 500 nm. (D) Histogram of measured carboxysome diameters in TEM data. Measured diameters are compared with a distribution model that considers bias induced by a TEM slice thickness less than an estimated carboxysome diameter of 150–250 nm (see *Materials and Methods*).

10-min intervals and quantified changes in fluorescence intensity during carboxysome assembly (Figure 4A). Assembly times were estimated based on the time it took a particle to go from the first spot in the automatically detected track that was ≥50% of its maximum intensity to the first value ≥95% of its maximum intensity. Automated particle tracking revealed that both CcmM isoforms assembled slowly, with a significantly different average assembly time of 15.09 ± 4.82 h ($n = 24$, error = SD) for green particles representing M58-mNeonGreen and M35-mNeonGreen, and 13.29 ± 5.48 h ($n = 24$, error = SD) for blue particles representing mTagBFP2-M58 (Wilcoxon signed-rank test, $p = 0.0174$; Figure 4B). The measured assembly time is longer than the ~6- to 7-h assembly time previously reported for RuBisCO (Chen *et al.*, 2013), perhaps because of differences in temperature or light levels during imaging, or because carboxysomes in this strain are larger than WT.

The current model of carboxysome assembly and structure suggests that the smaller M35 CcmM isoform may assemble a pre-carboxysome matrix of RuBisCO, before M58 assembly and shell recruitment. To assess whether CcmM isoforms from the *B-ccmM-N* strain had different temporal recruitment during the development of new carboxysomes, we compared the timing at which blue and green particles reached the first time point at ≥50%, 75%, and 95% of their maximum intensity in each particle track (Figure 4C). We found that, on a track-by-track basis, green particles tended to reach 50% of their maximum intensity 1.67 ± 2.74 h sooner than blue particles during the same carboxysome assembly. This difference was found to be statistically significant when tested against a hypothetical difference of zero (Wilcoxon signed-rank test $p = 0.008$, $n = 24$, error = SD). This is reflected as an increased difference between the time at 50%-max intensity of the blue signal and time at 50%-max intensity of the green signal on the plot (Figure 4C). No significant difference was found between the timing of blue and green particles reaching a point ≥75% (–0.22 ± 4.29 h) or ≥95% (–0.13 ± 3.78 h) of their maximum intensities during each assembly event (Wilcoxon signed-rank test, $p = 0.715$ and $p = 0.994$, respectively, $n = 24$, error = SD). In 22 of 24 tracked carboxysome assemblies, automatic tracking detected

blue particles before green. Consequently the more rapid accumulation observed of mNeonGreen signal cannot, in the majority of analyzed assembly events, be due to M35-N accumulating in the absence of the full-length B-M58-N isoform.

For verification that this apparent bias toward detecting blue fluorescent particles was not due to poor signal from the green channel, the average maximum intensities of particle tracks were compared between the channels. As expected from the reported brightness of mNeonGreen, tracks from the green channel were found to have significantly higher maximum intensities on average (41.5 ± 11.2 a.u.) compared with mTagBFP2 (33.6 ± 8.7 a.u.) (Wilcoxon signed-rank test, $p < 0.0001$, $n = 24$, error = SD). Furthermore, due to differences in maturation times between mTagBFP2 and mNeonGreen (~24 and <10 min, respectively), signal from mNeonGreen-tagged proteins was expected to be detectable at least as rapidly as signal from mTagBFP2 (Oksana *et al.*, 2011; Shaner *et al.*, 2013). A slower mTagBFP2 maturation time could also account for the observed faster accumulation of mNeonGreen. Together these data and analysis do not support a model of carboxysome assembly in which the short CcmM isoform M35 coordinates the RuBisCO lattice entirely in the absence of M58, suggesting instead that M58 may be involved in the early stages of organizing the inner carboxysome matrix.

M58 is not confined to a subshell layer in the carboxysome

Superresolution microscopy of dual-tagged CcmM suggests that M58 and M35 are indistinguishable in their distribution in the carboxysome. We used 3D-SIM to acquire superresolution images of the Δ*ccmM* + *B-ccmM-N* strain, RuBisCO tagged with a superfolder green fluorescent protein (RbcL-sfGFP), and two fluorescently tagged versions of the shell protein CcmK4 (CcmK4-mTagBFP2 and CcmK4-sfGFP) in PCC7942. The 3D-SIM images of strains with both GFP- and BFP-tagged CcmK4 laterally resolved the external carboxysome shell as a hollow ring (Figure 5, A and B), demonstrating that 3D-SIM provides sufficient resolution to visualize peripherally localized proteins in the carboxysome. To confirm these rings were not an artifact of 3D-SIM reconstruction, we imaged a strain of PCC7942 integrated
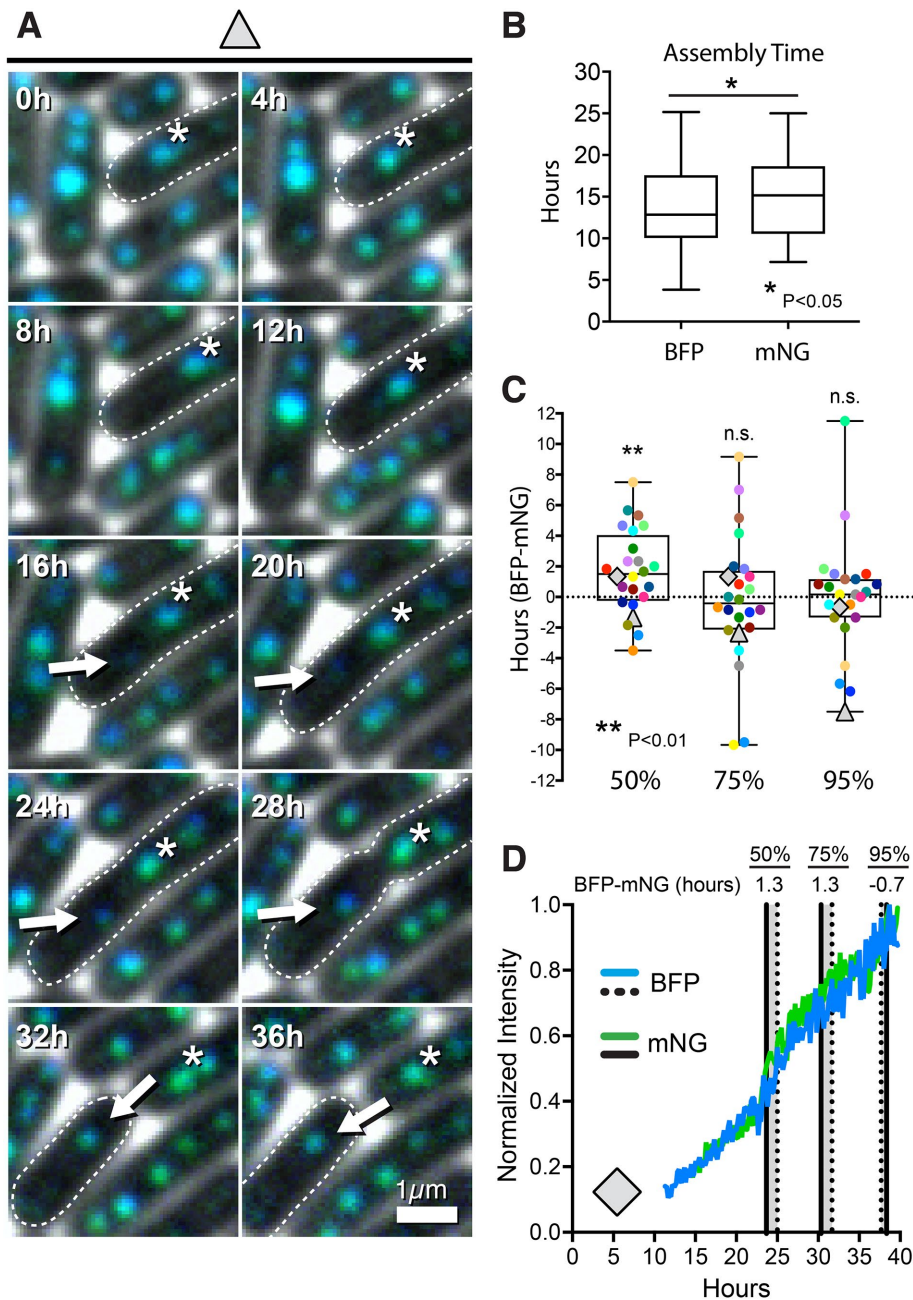
FIGURE 4: CcmM isoforms coassemble at the site of new carboxysomes. (A) Merged montage of carboxysome biogenesis in the Δ*ccmM* + *B-ccmM-N* gene complement strain shows simultaneous colocalization of both blue (mTagBFP2-M58) and green (M58-mNeonGreen/M35-mNeonGreen) particles. White arrows indicate the new carboxysome. White asterisk indicates the parent carboxysome. (B) Plot of carboxysome assembly times. Particle tracking during carboxysome assembly was used to determine changes in normalized blue and green particle intensities during assembly. Plots represent the time from the first point at which mTagBFP2 (BFP) and mNeonGreen (mNG) particle intensities were ≥50% to the point ≥95%. (C) Plot of temporal differences between normalized BFP and mNG intensities during carboxysome assembly. Plot depicts the difference in hours it took BFP and mNG particles to reach 50%, 75%, and 95% of their maximum intensity during a specific assembly event. Spots are color coded by carboxysome assembly event. Gray triangles correspond to the assembly event depicted in A. Gray diamonds correspond to the assembly event depicted in D. (D) Normalized tracks of representative carboxysome assembly event. Each particle track is normalized to its maximum intensity. Lines correspond to first points ≥50%, 75%, and 95%. Differences (BFP-mNG) are noted above each point. Statistical significance is denoted by asterisks (Wilcoxon signed-rank test).
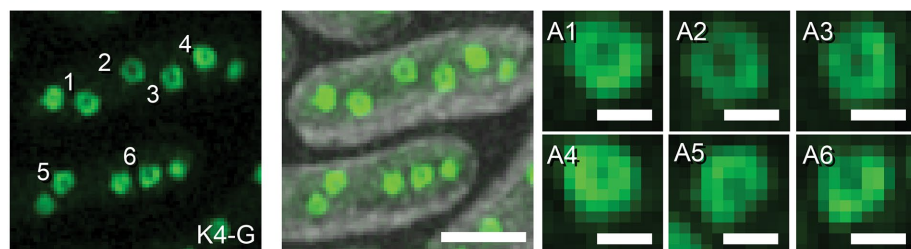
with a GFP-labeled copy of the large subunit of RuBisCO (RbcL-sfGFP). This strain has been previously used successfully to study RuBisCO assembly and spacing (Savage *et al.*, 2010; Chen *et al.*, 2013). 3D-SIM of RbcL-sfGFP (RbcL-G) showed no ringlike structures, producing only solid, regularly spaced particles (Figure 5C).

To test whether M58 was in fact limited to a subshell layer, we imaged the Δ*ccmM* + *B-ccmM-N* gene complement with 3D-SIM. Both CcmM isoforms predominantly produced solid objects similar to those observed with the RbcL-G strain (Figure 5D). Though infrequent, some large fluorescent particles with minor dips of intensity near their centers were observed by eye when imaging both isoforms (Figure 6, D and E). These qualitative results suggested that the tagged M58 isoform of CcmM was not significantly excluded from integration into the carboxysome core as would be expected if the protein was only present as a thin layer just beneath the exterior shell. To check that variations in signal intensity between experiments and cyanobacterial strains did not lead to poor signal-to-noise ratios and consequent artifacts, we verified the reconstruction quality of each 3D-SIM data set by the reconstructed intensity histogram (RIH) score from the SIMcheck ImageJ plug-in (Ball *et al.*, 2015). RIH scores for all conditions and data sets were of similar quality (Supplemental Table S1).
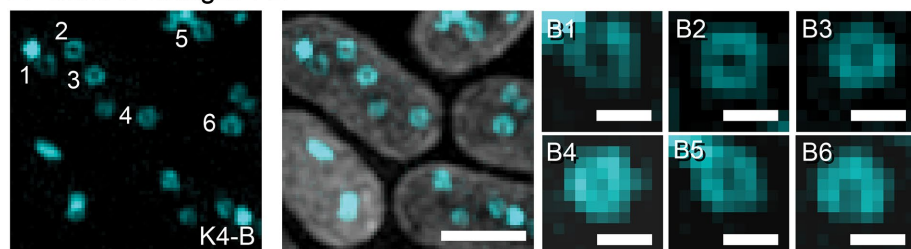
We developed an automated image analysis pipeline and a metric to quantify the degree to which fluorescently labeled proteins were localized at the perimeter of the carboxysome versus uniformly distributed throughout the matrix. The max-to-center intensity (MTC) ratio is calculated for each particle as the peak intensity of a polynomial curve fitted to an interpolated average radial profile, divided by the intensity at the particle centroid. A perfectly uniform protein distribution would result in the peak particle intensity near that of the particle centroid and yield an MTC ratio of ~1. Higher MTC values result from particles with decreased intensity at their centers, indicating a more ringlink appearance and a depletion of fluorescently labeled protein closer to the particle center (Figure 6). An estimate of particle size was calculated for each analyzed particle by taking the distance from the particle centroid to the peak intensity of the polynomial function fitted to the average radial profile. For objects with peak fluorescence at their centroid, this distance is 0. It should be noted that the "true" size of solid objects measured by the centroid-to-peak metric
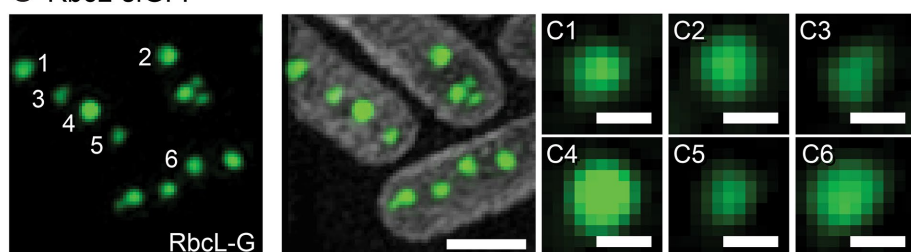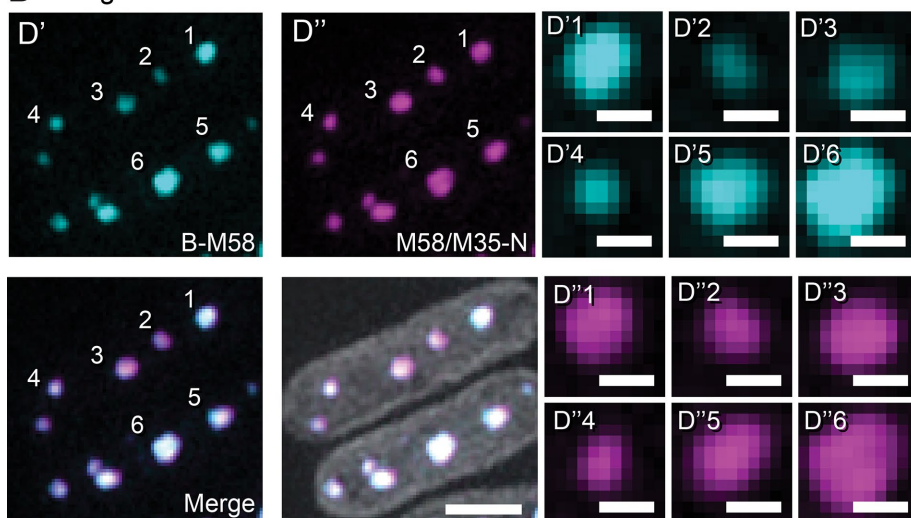
A CcmK4-sfGFP — K4-G — A1 A2 A3 A4 A5 A6

B CcmK4-mTagBFP2 — K4-B — B1 B2 B3 B4 B5 B6

C RbcL-sfGFP — RbcL-G — C1 C2 C3 C4 C5 C6

D mTagBFP2-CcmM-mNeonGreen — D′ B-M58 — D″ M58/M35-N — Merge — D′1 D′2 D′3 D′4 D′5 D′6 — D″1 D″2 D″3 D″4 D″5 D″6
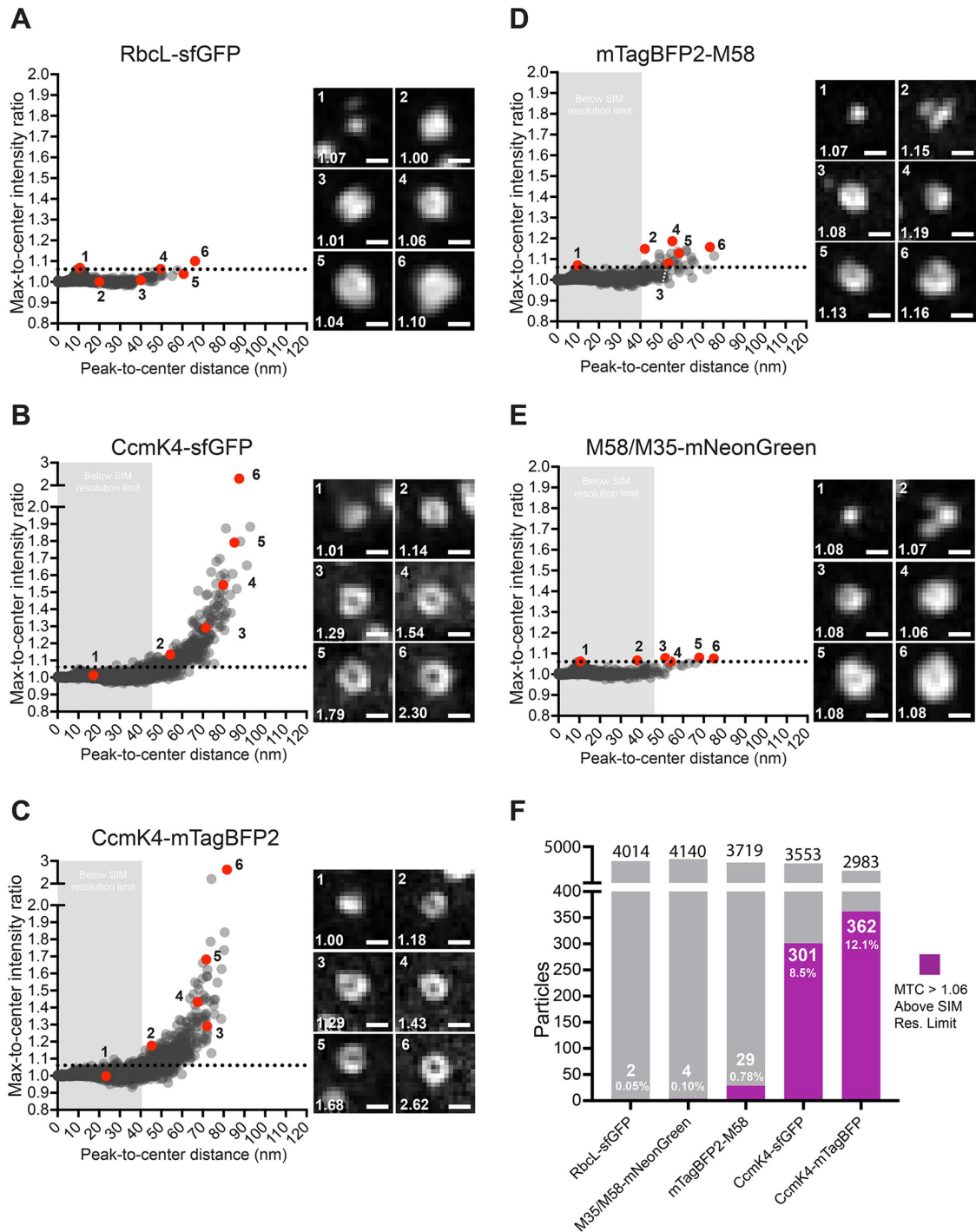
FIGURE 5: 3D-SIM of fluorescently tagged carboxysomes resolves the ring of the outer protein shell and an absence of shell-like localization in either RuBisCO or CcmM labeled strains. (A, B) 3D-SIM of K4-G and K4-B resolves the carboxysome shell as a hollow ring, while (C) 3D-SIM of RbcL-G produces solid particles. (D) 3D-SIM of ΔccmM + B-ccmM-N produces RuBisCO-like, apparently solid particles. M35/M58-N particles are pseudocolored magenta. Numbers identify individual carboxysomes and correspond to magnified panels on the right. Scale bars: 1 µm (large panels); 200 nm (small magnified panels).

on the Abbe resolution criterion for each fluorescent tag, below which we would not expect 3D-SIM to resolve even a "true" ring-like object (see *Materials and Methods*). Diffraction-limited peak-to-center distances were defined as 44.89, 45.51, and 39.96 nm for sfGFP, mNeonGreen, and mTagBFP2, respectively (Figure 6, shaded areas).

Analysis of variance (ANOVA) testing confirmed that mean MTC values were significantly heterogeneous between all the labeled carboxysome proteins (Welch's ANOVA, $F_{4, 8302.6} = 103.90$, $p < 0.001$). A Games-Howell test with $q_{critical}$ ($k = 5$, $df = \infty$, $\alpha = 0.001$) = 5.484 was then used to make further pairwise comparisons of labeled carboxysome protein MTC values (Supplemental Table S2). This automated analysis of RbcL-G and CcmK4-sfGFP (K4-G) images confirmed our initial observations that carboxysomes appear fundamentally different between these strains (Games-Howell test, MD = 0.02, $q = 17.65$); similar results were obtained from the comparison of RbcL-G and CcmK4-mTagBFP2 (K4-B) (Games-Howell test, MD = 0.02, $q = 21.09$). RbcL-G particles had an average MTC ratio of 1.008 ± 0.011, with a maximum MTC ratio of 1.10 ($n = 4014$, error = SD). An upper MTC ratio threshold was set at 1.06, which is the 99.9th percentile of the RbcL-G MTC ratio scores, below which objects are more likely to be uniform and non-ringlike. This threshold is denoted on MTC ratio versus peak-to-center distance plots as a horizontal dotted line (Figure 6). Particles with MTC ratios greater than 1.06 were only counted as rings if the distance from centroid to the point of maximum intensity was greater than the fluorophore-specific 3D-SIM resolution limit. We found that a subset of carboxysomes with MTC >1.06 were measured with peak-to-center distances *below* the theoretical 3D-SIM resolution limit in both K4-G cells (14 subresolution rings) and K4-B cells (29 subresolution rings). Manual inspection of these subresolution rings revealed that they frequently had misidentified centroids, often due to rotationally asymmetrical fluorescence intensity (Supplemental Figure S3). Centroid misidentification may result in underestimation of particle size, as the centroid will be called inappropriately close to the point of maximum intensity in the particle average radial profile. While subresolution rings were not counted as true rings, their measured sizes were on average very near their respective 3D-SIM resolution limits. K4-G subresolution rings had an average radius of 41.1 ± 4.5 nm, near the 44.89 nm limit ($n = 14$, error = SD). Similarly, K4-B subresolution rings had an average radius of 35.0 ± 4.8 nm, which

would likely be underestimated, but their ringlike character would not be. Because the theoretical 3D-SIM resolution limit depends on fluorophore wavelength, particle size cutoffs were calculated based

FIGURE 6: Analysis of 3D-SIM data. MTC intensity ratios measure the degree to which a fluorescent object is resolved as a ring. (A–E) Peak-to-center distance versus MTC ratio plots for all labeled carboxysome strains. Horizontal dotted lines denote an upper MTC threshold, below which particles are expected to be solid and uniform. This threshold was calculated from the maximum measured MTC score in RbcL-G data. Inset images correspond to red dots in each panel. Insets: scale bars = 200 nm; numbers denote MTC ratios. (F) Summary of MTC analysis from all labeled carboxysome strains. Gray bars depict total analyzed particles, with totals labeled above each bar. Purple bars depict particles with MTC scores >1.06 that were also above respective 3D-SIM resolution limits, with corresponding counts and the percent of total labeled in white.

is near the mTagBFP2 resolution limit of 39.96 nm ($n = 29$, error = SD). On the basis of the small number of subresolution rings, their close proximity to the 3D-SIM resolution limit, and the marked increased in MTC scores past this limit, we conclude that we were

able to resolve rings very near the ~110-nm theoretical lateral resolution limit of 3D-SIM (at 520-nm wavelength; Gustafsson, 2000; Gustafsson *et al.*, 2008) and can reliably resolve fluorescent points less than 200 nm apart, which is well below the average diameter

of carboxysomes found in the *B-ccmM-N* strain as measured by TEM (~319 nm).

In contrast to RbcL, we found that fluorescently labeled shell proteins produced high MTC ratios. Compared with RbcL-G, K4-G particles had a significantly greater average MTC ratio of 1.023 ± 0.073 (*n* = 3553, error = SD; Figure 6B). In cells with K4-G–labeled carboxysomes 8.5% (301 of 3553) of particles had MTC ratios >1.06 above the sfGFP 3D-SIM resolution limit, denoting a decrease in fluorescently labeled protein toward the particle center (Figure 6F). This was also true for cells with K4-B–labeled carboxysomes, which produced particles with a significantly different mean MTC ratio of 1.030 ± 0.080 compared with RbcL-G (*n* = 2983, error = SD; Figure 6C). In the K4-B strain, 12.1% of particles (362 of 2983) had MTC scores >1.06 and had measured radii above the mTagBFP2 3D-SIM resolution limit.

The mean MTC ratios of labeled carboxysomes in K4-B and K4-G cells were also found to be significantly different (Games-Howell test, α = 0.01, MD = 0.007, *q* = 4.884). This corresponded to a greater number of rings identified in K4-B cells compared with K4-G (12.1% vs. 8.5%, respectively). This difference may be the result of an improvement in resolution due to the shorter wavelength of blue versus green fluorophores (Figure 6F). Together the comparative analysis of carboxysomes with fluorescently labeled RbcL or CcmK4 shell proteins verified that 3D-SIM could resolve the carboxysome shell as a hollow ring and that such rings were absent in cells with fluorescently labeled RuBisCO.

Analysis of the Δ*ccmM* + *B-ccmM-N* gene complement identified a small number of fluorescently tagged M58 particles as ringlike (Figure 6D). Our analysis found only 0.78% (29 of 3719) of the mTag-BFP2-M58 (B-M58) particles had MTC ratios >1.06 and were above the 3D-SIM resolution limit, an ~11-fold decrease in percent compared with K4-G and a 16-fold decrease compared with K4-B, with an average MTC ratio of 1.009 ± 0.014 (*p* < 0.01, error = SD; Figure 6D). We found a significant difference in the MTC ratios of B-M58 particles versus both shell-labeled K4-B (Games-Howell test, MD = 0.020, *q* = 19.49) and K4-G (Games-Howell test, MD = 0.014, *q* = 15.74). This supported qualitative observations that particles of the labeled M58 strain did not appear as ringlike as those in the strains with labeled carboxysome shells.

The maximum MTC score found in B-M58 particles was only 1.19 compared with 2.30 in K4-G and 2.62 in K4-B particles. In fact, 37% of K4-G and 27% of K4-B ringlike particles (MTC >1.06) were scored above the max B-M58 score. B-M58 particles also had significantly different MTC ratios compared with RbcL-G particles (Games-Howell test, MD = 0.002, *q* = 7.49). Taken together, these test results indicate that, though B-M58–labeled carboxysomes have a small number of MTC ratios ≥1.06 with radii above the 3D-SIM resolution limit, and thus have resolvable dips of intensity toward their centers, this dip is frequently not as large as that of many (~30%) shell-labeled carboxysomes.

The Δ*ccmM* + *B-ccmM-N* complement, which expresses both full-length M58-mNeonGreen and the short isoform M35-mNeonGreen (M58/M35-N), produced four particles with MTC ratios ≥1.06 above the 3D-SIM resolution limit, and had an average MTC ratio of 1.007 ± 0.010 (*n* = 4140, error = SD; Figure 6, E and F). The mean MTC ratio of these particles was significantly different from those of both labeled K4-G (Games-Howell test, MD = 0.016, *q* = 18.02) and K4-B (Games-Howell test, MD = 0.022, *q* = 21.39). Pairwise comparison of M58-mNeonGreen and M35-mNeonGreen particles to RbcL-G found no significant difference in mean MTC ratios (Games-Howell test, MD = 0.0003, *q* = 1.86). These data indicated that the population of green fluorescent particles produced in the Δ*ccmM* + *B-ccmM-N* strain were

predominantly solid, like those observed in the strain with labeled RuBisCO.

DISCUSSION

Dual fluorescent tagging of CcmM alters relative isoform abundance

The dual-fusion *B-ccmM-N* transgene effectively produced both long and short CcmM isoforms. Though M35 remained more abundant than M58, we observed a reduced level of M35 expression in the transgenic line relative to levels in WT cells. It is important to note that this change in the relative amount of each isoform may have had an impact on the assembly and structure of the carboxysomes produced in these cells, as suggested by their larger average size. It is possible that a more equivalent ratio of M35 to M58 may result in a situation in which the cell must use more M58 to organize the internal RuBisCO matrix than it would under normal conditions. Despite this change in isoform ratio, tagged CcmM isoforms can still assemble functional carboxysomes that support growth at atmospheric levels of CO_2. If internal protein organization is significantly abnormal in carboxysomes of these cells, their relatively normal functionality suggests that the carboxysome structure is highly flexible to changes in CcmM abundance. This raises the question of to what extent CcmM isoform expression may regulate carboxysome size, number, and internal protein organization.

The carboxysome can support the addition of large foreign proteins via direct fusion to CcmM

The function of CcmM and other components of the carboxysome are robust to the addition of large protein fusions, further supporting a tagging strategy as a means to localize foreign cargo to the carboxysome for engineering applications. Previous work has shown that tagged CcmM gene complements can rescue the HCR phenotype of CcmM mutants without significant impairment of carboxysome function compared with WT cells (Long *et al.*, 2010; Cameron *et al.*, 2013). We find that such complementation is also possible when fluorescent tags are fused to both ends of CcmM, significantly increasing the size of both the M58 and M35 isoforms. These results suggest that heterologous proteins could be simultaneously fused to multiple loci in the matrix, opening the door for localizing multipart enzymatic pathways inside the carboxysome.

M35 and M58 assemble simultaneously during early carboxysome biogenesis in the dual-fusion CcmM strain

M35 has been hypothesized to coordinate the organized paracrystalline cargo assembly of RuBisCO, with M58 limited to a peripheral subshell layer (Long *et al.*, 2007, 2010, 2011; Cot *et al.*, 2008; Rae *et al.*, 2013). Current models of carboxysome biogenesis have proposed a primarily cargo-centric assembly pathway, in which RuBisCO and internal structural components form before shell encapsulation (Cameron *et al.*, 2013; Chen *et al.*, 2013). On the basis of fluorescence recovery after photobleaching imaging of carboxysomes that suggests matrix components are relatively static (Chen *et al.*, 2013), we hypothesized that M35 would be present in pre-carboxysome assemblies before M58, with M58 appearing later during shell formation. Indeed, we do observe a significant difference in fluorophore dynamics early on in carboxysome assembly, with mTagBFP2 fluorescence, specific to the long M58 isoform, accumulating more slowly than that of mNeonGreen. This difference becomes insignificant later in the assembly. The slower accumulation of blue fluorescence during carboxysome assembly in the Δ*ccmM* + *B-ccmM-N* cells, specifically marking the M58 isoform, raises the possibility that M35 may play a more central role than M58 during the initial stages

of RuBisCO organization. However, mNeonGreen was detected only before mTagBFP2 in 2 of 24 analyzed carboxysome assemblies, despite mNeonGreen having higher particle intensities. Thus, within the temporal limitations of this experiment it is unlikely that the observed difference in accumulation rates is representative of M35 coordinating early carboxysome assembly in the absence of M58. Rather, because both isoforms appear to always be present together to some degree, it is more likely that a faster accumulation of green fluorescence is due to both long and short mNeonGreen-labeled isoforms assembling simultaneously. Consequently, though these findings do not directly contradict the current models of carboxysome assembly, in which cargo-centric assembly is driven by M35, these experiments suggest that both M35 and M58 are integrally involved in the structuring of the internal matrix during carboxysome assembly. Assuming that the carboxysome core grows by addition of material to the outside of a stable paracrystalline RuBisCO assembly (Chen *et al.*, 2013), these results also suggest that M58 does not assemble as a separate layer around a preexisting M35/RuBisCO core.

M58 is not exclusive to a subshell layer in the Δ*ccmM*, *mTagBFP2-ccmM-mNeonGreen* strain

The 3D-SIM experiments and quantitative analysis do not support a model of carboxysome internal structure in which M58 is exclusively limited to a subshell localization. The preexisting model described earlier proposes that M58 is not present within the primary M35-RuBisCO matrix. This is logical, because M35, which does not contain the N-terminal domain, presumably can achieve denser packing of RuBisCO enzymes.

We expected that, if M58 was in fact limited to a subshell layer ~5–6 nm beneath the outer surface, it would appear as a ring, similar to CcmK4, by 3D-SIM (Kaneko *et al.*, 2006). While 3D-SIM imaging of CcmK4 did reveal the expected ringlike distribution, carboxysomes with fluorescently labeled M58 (B-M58) appeared predominantly as solid objects, with only a minor population (0.8%) showing dips in fluorescence intensity at their centers. Consequently we do not find strong evidence by superresolution microscopy to support a model of carboxysome structure in which M58 is strictly excluded from the carboxysome core, suggesting that the internal carboxysome structure contains a mixed population of both M35 and M58 coordinating with RuBisCO. We cannot rule out, however, the possibility that there are distinct layers of M35 and M58 deeper within the carboxysome interior, below the 3D-SIM resolution limit. Furthermore, because there is strong evidence indicating that M58 is required to directly recruit shell proteins, it may likely be locally enriched near the shell. Such enrichment would not have been detectable with the experimental design we employed in this study. While it is also possible that fluorescently tagging these proteins may perturb their natural organization, the lack of a major growth defect in our tagged strain suggests that, if there are differences in organization, they are not essential to carboxysome function.

Though 3D-SIM provides lateral and axial resolution doubling, our method does have its limitations. Like conventional microscopy, axial resolution in 3D-SIM is worse than lateral resolution. Carboxysomes are three-dimensional icosahedra with a diameter (~200 nm) that is above the lateral 3D-SIM resolution limit (~110 nm) but below the axial resolution limit (~340 nm). Thus we would expect slightly decreased contrast, noisier measurements, and reduced ability to resolve the true "dip" in intensity in the hollow interior of a carboxysome than with a true two-dimensional ring of fluorescence. In our method, we averaged radial intensities across five 0.5-pixel subsampled z-planes around the centroid and then took an average of these when analyzing particle intensity. While increasing the robustness of the method, this may have also increased the minimum resolvable shell diameter. Nonetheless, the effective resolution of this method was sufficient to demonstrate differences in distribution of CcmK4, RuBisCO, M58, and M35. Even with the limitations of 3D-SIM, we have demonstrated that this technique, coupled with computational analysis, can provide a powerful tool for studying protein organization in large multi-protein structures. The finding that M58 may be present throughout the carboxysome core raises questions about the compartment's internal structure. For example, CcmM has been reported to interact with other carboxysome components (such as CcaA, CcmN, and CcmK) in yeast two-hybrid and pull-down experiments (Long *et al.*, 2007; Cot *et al.*, 2008; Kinney *et al.*, 2012), although the strength of these interactions is unknown. CcmN is essential for shell recruitment and assembly (Kinney *et al.*, 2012) and thus is thought to localize at the carboxysome periphery (Rae *et al.*, 2013). In addition, crystal structures of CcmM from *Thermosynechococcus elongatus* have revealed a homotrimer complex (Peña *et al.*, 2010). Thus CcmM may be involved in multiple structural and functional roles throughout the carboxysome (Figure 7).

Our findings also raise new questions about the structure and biogenesis of carboxysomes. For example, M58 is thought to play a role in recruitment of shell components (Cot *et al.*, 2008; Long *et al.*, 2011; Kinney *et al.*, 2012; Cameron *et al.*, 2013).
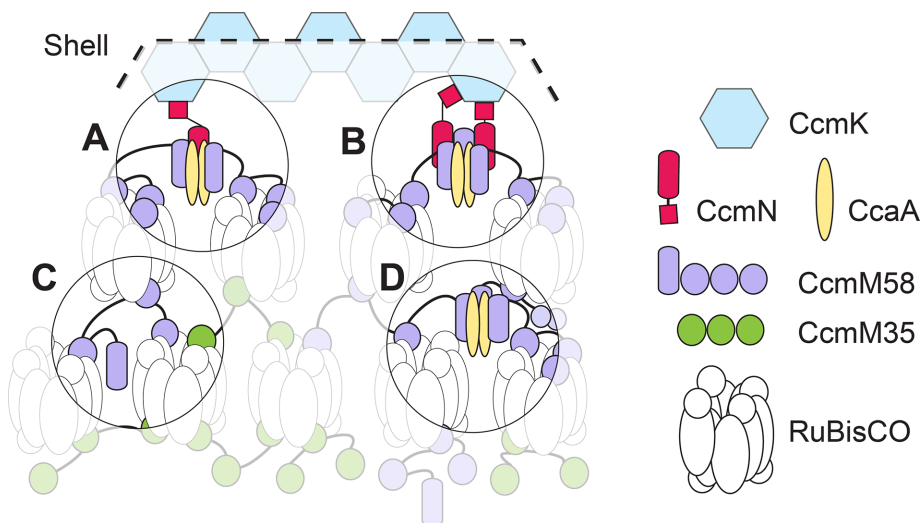
FIGURE 7: Model of possible structural and functional roles of CcmM in the *S. elongatus* β-carboxysome. (A, B) Full-length CcmM may form trimeric complexes through N-terminal interactions, which most likely include CcaA. Based on structural similarity between N-terminal domains of CcmN and CcmM, CcmN may be directly displacing units of CcmM in this complex or binding the trimer to coordinate exterior shell recruitment (Kinney *et al.*, 2012). (C, D) We find evidence supporting a model in which full-length CcmM58 is also present within the core of the carboxysome, which may involve single units of CcmM58 coordinating multiple RuBisCO enzymes as in C or may mean that CcmM58 is forming trimeric complexes within the interior as illustrated in D. Protein illustrations based on Rae *et al.* (2013).

However, shell proteins are recruited to carboxysomes only late in their assembly process (Chen *et al.*, 2013). Therefore, if M58 is present even at the early stages of carboxysome assembly, other factors must be responsible for delaying shell recruitment. Furthermore, as our data indicate that CcmM58 is present deep within the carboxysome, it is possible that this protein is interacting with the CA CcaA throughout the internal matrix of RuBisCO (Figure 7D). The nature of these factors is a promising avenue for future work.

MATERIALS AND METHODS
Western blot analysis
For SDS–PAGE, log-phase (OD_{750} = 1.0) cultures of cyanobacterial strains were pelleted and frozen at −20°C. Frozen pellets were thawed in B-PER Bacterial Protein Extraction Reagent (ThermoScientific), without DNase or Lysozyme, and normalized by wet pellet mass. Resuspended cells were mixed directly with SDS loading buffer and boiled. Boiled samples were run on a 4–20% Tris-glycine NuPAGE gel (Invitrogen) at 120 V. SDS–PAGE–separated proteins were transferred to a nitrocellulose membrane with an iBlot2 transfer device (ThermoScientific).

The membrane was blocked with 5% skim milk in TBST (50 mM Tris, 150 mM NaCl, 0.1% Tween 20), then probed with 1:10,000 of anti-CcmM primary antibody (serum derived from rabbit, a gift of Ben Long, Australian National University), followed by a horseradish peroxidase–conjugated goat anti-rabbit secondary antibody (Agrisera AS09 602). The membrane was incubated with SuperSignal West Dura Extended Duration chemiluminescent substrate (ThermoScientific) and imaged with the Bio-Rad ChemiDoc system.

Western blotting for CcmM in WT, mutant, and transgenic cyanobacterial strain was replicated in two separate experiments, performed on different days, with independently collected culture samples (Supplemental Figure S1).

TEM
For TEM experiments, mid–log cultures (1 ml) were pelleted (6000 rpm, 5 min) and concentrated 2× in sterile dH_2O. The cells were then mixed 1:1 with fixative (1.25% formaldehyde, 2.5% glutaraldehyde, 0.03% picric acid, 0.1 M sodium cacodylate buffer, pH 7.4), incubated at room temperature for 30 min, and then pelleted and stored in fixative at 4°C overnight. Fixed cells were embedded in Epon resin and cut into ultrathin sections (~60–80 nm). Sections were stained with uranyl acetate and lead citrate, then imaged on a Tecnai G2 Spirit Bio TWIN TEM.

Carboxysome diameter was measured manually in ImageJ. For estimating how a section thickness less than the width of a typical carboxysome would influence this measurement, a model distribution of carboxysome diameter was generated. A theoretical sample of 50 objects with diameters between 150 and 250 nm were generated. The observed widths of these objects were calculated based on randomly selected points, representing a slice through a carboxysome, that were less than or equal to each object's full diameter. This point was then used to calculate the measured width of the object slice. Measurements less than 100 nm were judged to be too small to have been considered true carboxysomes in the TEM data and were excluded from the model.

Cell culture
WT, mutant, and modified strains of *Synechococcus elongatus* PCC7942 were grown in BG-11 media (Sigma), with 1 g/l HEPES adjusted to pH 8.5. Cultures were grown at 30–35°C under constant light with an approximate intensity of 1000 lm/m^2. Cultures were grown in 20–40 ml BG11 media in 125- or 250-ml flat-bottom flasks,

shaking at 150 rpm in an INFORS Multitron 2 incubator, which features digital CO_2 control. WT 7942 and knockout complements were grown with ambient air conditions. Mutant Δ*ccmM*::*HygR* cultures were supplemented with 2% CO_2 flowed through the incubator headspace and 25 µg/ml hygromycin B. Strains with fluorescently labeled carboxysome components, carrying kanamycin or spectinomycin resistance genes, were grown with 25 µg/ml kanamycin or 25 µg/ml spectinomycin, respectively. For the CcmM complement strain, Δ*ccmM* + *B-ccmM-N*, cultures were grown with 5 µg/ml kanamycin and 25 µg/ml hygromycin B. For growth-curve experiments, biological replicates were made by isolating colonies grown on BG11 agar with 1 g/l HEPES, 50 mM HCO_3^-, and 1 mM $Na_2S_2O_3$. Two independent growth experiments were performed starting on different days, with three replicates in each experiment for a total of six biological replicates. One replicate of WT 7942 grown in 2% CO_2 group was excluded due to significant evaporation in the culture. Isolates were screened by PCR to confirm the presence or absence of the WT *ccmM* gene. Growth-curve cultures were prepared by washing starter cultures in fresh BG11 pH 8.5 media, then diluting to OD_{750} of ~0.1 in 40 ml BG11 in 250-ml flat-bottom flasks. To calculate approximate strain-doubling times (*d*), we used the formula $d = t \star \log 2 / (\log OD_f / \log OD_o)$ with OD_{750} measurements from 0 to 18 h. A log transformation of growth data verified that measurements at these times were approximately linear with later time points, indicating these were not in a lag phase of growth (Supplemental Figure S4).

Image acquisition
For both conventional fluorescence and 3D-SIM experiments, 5 µl of either mid-log cells (OD_{750} = 1–2) for time-lapse experiments or early-log cells (OD_{750} = 0.5–1.2) for 3D-SIM were spotted on 2% agarose BG11 pads. Agarose pads were placed sample-side down in MatTek 35-mm glass-bottom microwell dishes with No. 1.5 coverslips. Sterile water was spotted within the dish to mitigate dehydration of the agarose pad, and the dish was sealed with parafilm. Though strains expressing labeled CcmM were under the control of the IPTG-inducible promoter P*trc*, no induction was used with these cells due to adequate basal expression. Cells expressing RbcL-G were imaged on BG11 agarose pads with the addition of 50 µM IPTG following previously reported protocols (Savage *et al.*, 2010). 3D-SIM of uninduced RbcL-G cells also produced solid particles, but these were not as bright as those seen with induced cells and produced several false positives in our analysis pipeline (Supplemental Figure S5). For time-lapse experiments, samples were recovered for more than 1 h at 34–35°C, under ~1000 lm/m^2, and in ambient air before being imaged using a Nikon TE2000 and a 100× oil objective. Cells were kept at 30°C under ~800 lm/m^2 light intensity during time lapse and imaged every 10 min.

The 3D-SIM data were collected on a DeltaVision OMX V4 Blaze system (GE Healthcare) equipped with a 60×/1.42 NA Plan-Apo oil-immersion objective lens (Olympus) and three Edge 5.5 sCMOS cameras (PCO). mTagBFP2 fluorescence was excited with a 405-nm laser and collected with a 477/35 emission filter, mNeonGreen with a 514-nm laser and 541/22 emission filter, and sfGFP with a 488-nm laser and a 528/48 emission filter. z-Stacks of ~2 microns were acquired with a z-step of 125 nm and with 15 raw images per plane (five phases, three angles). Spherical aberration was minimized using immersion-oil matching (Hiraoka *et al.*, 1990). Superresolution images were computationally reconstructed from the raw data sets with a channel-specific measured optical transfer function and a Wiener filter constant of 0.001 using Compute Unified Device Architecture (CUDA) accelerated

3D-SIM reconstruction code based on Gustafsson *et al.* (2008). TetraSpeck beads (Thermo Fisher) or a nano-grid control slide were used to measure axial and lateral chromatic misregistration, and multichannel data sets were registered using the image registration function in softWoRx. The 3D-SIM data sets of each strain used for quantitative analysis were acquired in two independent experiments that were performed with samples prepared on different days.

Image analysis

3D-SIM data sets were imported into MATLAB (MathWorks) using the bioformats reader, followed by thresholding and background subtraction. The threshold value was empirically determined and assessed by visualizing the resultant centroid position and mask in MATLAB and Imaris (Bitplane AG), respectively. Segmented objects were further analyzed if they met a cutoff for volume, surface area, sphericity, major–minor axis ratio, and mean radius.

We calculated the MTC (max to center) ratio for each object. From the centroid, the radially averaged intensity for each subsampled (0.5 pixels) radius was measured. This was done at the particle centroid and one 0.5-pixel subsampled *z*-plane above and below for five total planes. Radial profiles were averaged across *z*-planes. A polynomial curve was fitted to the averaged radial profile of each segmented object in MATLAB. The most suitable polynomial fit (up to sixth order) was selected based on meeting the Bayesian information criterion. Then the first and second derivatives of each fitted curve were calculated to find the root with the global maximum. The intensity at this root was calculated and divided by the intensity at the centroid to obtain particle MTC ratios. An estimation of particle size was also made by taking the distance from the global max of the fitted polynomial to the particle centroid. For subdiffraction objects with peak intensities at their centers, this resulted in a distance of 0 nm. After polynomial fitting, a small number of particles (<0.4%) in each strain were calculated to have MTC ratios <0.4. While many particles have MTC ratios between 0.9 and 1, these were the only ones found to have scores less than 0.9. Visual analysis revealed that these were artifacts of curve fitting in which small local maxima were generated that fell well below the particle centroid intensity. All particles with MTC <0.4 had MTC ratios of 1 when the max of the initial averaged radial profile was used instead of the fitted polynomial. To correct for this, these particles were forced to an MTC ratio of 1.0 with a distance to peak intensity of 0. Importantly, complete exclusion of these particles does not alter our conclusions or the statistical test results. The 3D-SIM resolution limits were calculated for each fluorophore using the Abbe criterion divided by a factor of 2 to account for the twofold increase in lateral resolution with 3D-SIM: $(0.5 \times \lambda em)/(2 \times NA_{1.42})$ (λem = emission wavelength, NA = numerical aperture; Pédelacq *et al.*, 2006; Oksana *et al.*, 2011; Shaner *et al.*, 2013).

Time-lapse data of Δ*ccmM* + *B-ccmM-N* were processed with ImageJ (FIJI) (Schindelin *et al.*, 2012). Time-lapse data from two sequential acquisitions of the same field of view were imported into FIJI with the Bio-Formats Import plug-in with autoscaling, concatenated, and separated by channel. Channels were registered using rigid registration in the StackReg FIJI plug-in, then background subtracted with a 50-pixel-radius rolling ball. Particle tracking was performed in FIJI with the TrackMate plug-in using the LoG detector (Laplacian of Gaussian filter) with 0.5-μm estimated blob diameter, 0.5 threshold, and subpixel localization (Tinevez *et al.*, 2017). Tracks were generated with a maximum linkage and gap-closing distances of 0.5 μm and with a maximum

frame gap of 2. Tracks were manually checked for gaps and incorrect splitting. False splits and gaps were manually corrected. Particle tracks were corrected for photobleaching by dividing intensities by an average of seven reference particles, normalized to the first frame of the time lapse, in each channel. Reference particles were objects observed to be relatively stable compared with particles that lost or gained fluorescence due to carboxysome biogenesis. The same reference particles were used for correction in both channels. Bleach-corrected tracks were normalized to their maximum intensity. To quantify and compare differences in assembly dynamics between blue and green fluorescence signals, we selected reference points at 50%, 75%, and 95% of maximum intensity for each fluorophore in each assembly track. The percent assembly reference point was selected as the first point in the track that was greater than or equal to that reference point. Tracks that began with intensities greater than 50% of their maximum intensity in either channel were judged to be incomplete or false-assembly events and were discarded. For generation of the time-lapse montage, brightness and contrast values were manually adjusted separately in each channel to enhance visibility in the figure.

Cloning and strain construction

Plasmids used for *S. elongatus* strain construction were made by Gibson assembly and sequence verified. Tagged CcmM plasmids were cloned by inserting the *ccmM* gene, along with mNeonGreen and mTagBFP2 coding sequences with additional flexible linker sequences, into the previously described pDFS21 neutral site II (NS2) integration plasmid downstream of the IPTG-inducible P*trc* promoter (Savage *et al.*, 2010). The *ccmM* gene was obtained directly from the *S. elongatus* PCC7942 genome via PCR with Phusion polymerase (NEB). The *ccmK4* gene for cloning shell fusion plasmids was obtained as a synthesized gBlock (IDT) and cloned into the pDFS21 integration plasmid (Supplemental Tables S3 and S4). Annotated plasmid sequences have been provided as Supplemental Files.

The *S. elongatus* strains were transformed with integration plasmids by incubating approximately fivefold concentrated OD_{750} 1–2 culture with 10–100 ng plasmid at 30°C in the dark overnight; this was followed by plating of transformants on selective BG11 agar (Clerico *et al.*, 2007). The mutant Δ*ccmM* strain was made by integrating a hygromycin B resistance gene into the native *ccmM* ORF; this was followed by selective plating and screening (Sachdeva, 2014).

REFERENCES

Andersson I, Backlund A (2008). Structure and function of Rubisco. Plant Physio Biochem 46, 275–291.

Badger MR, Price GD (2003). CO_2 concentrating mechanisms in cyanobacteria: molecular components, their diversity and evolution. J Exp Bot 54, 609–622.

Ball G, Demmerle J, Kaufmann R, Davis I, Dobbie IM, Schermelleh L (2015). SIMcheck: a toolbox for successful super-resolution structured illumination microscopy. Sci Rep 5, 15915.

Cameron JC, Wilson SC, Bernstein SL, Kerfeld CA (2013). Biogenesis of a bacterial organelle: the carboxysome assembly pathway. Cell 155, 1131–1140.

Chen AH, Robinson-Mosher A, Savage DF, Silver PA, Polka JK (2013). The bacterial carbon-fixing organelle is formed by shell envelopment of preassembled cargo. PLoS ONE 8, e76127.

Clerico EM, Ditty JL, Golden SS (2007). Specialized techniques for site-directed mutagenesis in cyanobacteria. Methods Mol Biol 362, 155–171.

Cot SS, So AK, Espie GS (2008). A multiprotein bicarbonate dehydration complex essential to carboxysome function in cyanobacteria. J Bacteriol 190, 936–945.

Gustafsson MGL (2000). Surpassing the lateral resolution limit by a factor of two using structured illumination microscopy. J Microsc 198, 282–87.

Gustafsson MGL, Shao L, Carlton PM, Wang CJR, Golubovskaya IN, Cande WZ, Agard DA, Sedat JW (2008). Three-dimensional resolution doubling in wide-field fluorescence microscopy by structured illumination. Biophys J 94, 4957–4970.

Hiraoka Y, Sedat JW, Agard DA (1990). Determination of three-dimensional imaging properties of a light microscope system. Partial confocal behavior in epifluorescence microscopy. Biophys J 57, 325–333.

Kaneko Y, Danev R, Nagayama K, Nakamoto H (2006). Intact carboxysomes in cyanobacterial cell visualized by Hilbert differential contrast transmission electron microscopy. J Bacteriol 188, 805–808.

Kerfeld CA, Melnicki MR (2016). Assembly, function and evolution of cyanobacterial carboxysomes. Curr Opin Plant Biol 32, 66–75.

Kinney JN, Salmeen A, Cai F, Kerfeld CA (2012). Elucidating essential role of conserved carboxysomal protein CcmN reveals common feature of bacterial microcompartment assembly. J Biol Chem 287, 17729–17736.

Long BM, Murray BR, Whitney SM, Price GD (2007). Analysis of carboxysomes from Synechococcus PCC7942 reveals multiple Rubisco complexes with carboxysomal proteins CcmM and CcaA. J Biol Chem 282, 29323–29335.

Long BM, Rae BD, Badger MR, Price GD (2011). Over-expression of the β-carboxysomal CcmM protein in Synechococcus PCC7942 reveals a tight co-regulation of carboxysomal carbonic anhydrase (CcaA) and M58 content. Photosynth Res 109, 33–45.

Long BM, Tucker L, Badger MR, Price GD (2010). Functional cyanobacterial β-carboxysomes have an absolute requirement for both long and short forms of the CcmM protein. Plant Physiol 153, 285–293.

Oksana MS, Cranfill PJ, Davidson MW, Verkhusha VV (2011). An enhanced monomeric blue fluorescent protein with the high chemical stability of the chromophore. PLoS ONE 6, e28674.

Pédelacq JD, Cabantous S, Trans T, Terwilliger TC, Waldo GS (2006). Engineering and characterization of a superfolder green fluorescent protein. Nat Biotech 24, 79–88.

Peña KL, Castel SE, Araujo C, Espie GS, Kimber MS (2010). Structural basis of the oxidative activation of the carboxysomal γ-carbonic anhydrase. CcmM. Proc Natl Acad Sci USA 107, 2455–2460.

Price GD, Howitt SM, Harrison K, Badger MR (1993). Analysis of a genomic DNA region from the cyanobacterium Synechococcus sp. Strain PCC7942 involved in carboxysome assembly and function. J Bacteriol 175, 2871–2879.

Rae BD, Long BM, Badger MR, Price GD (2012). Structural determinants of the outershell of β-carboxysomes in Synechococcus elongatus PCC7942: roles for CcmK2, K3-K4, CcmO, and CcmL. PLoS ONE 7, e43871.

Rae BD, Long BM, Badger MR, Price GD (2013). Functions, compositions, and evolution of the two types of carboxysomes: polyhedral microcompartments that facilitate CO_2 fixation in cyanobacteria and some proteobacteria. Microbiol Mol Biol Rev 77, 357–379.

Sachdeva G (2014). Controlling Fluxes for Microbial Metabolic Engineering. Doctoral Dissertation. Cambridge, MA: Harvard University.

Savage DF, Afonso B, Chen AH, Silver PA (2010). Spatially ordered dynamics of the bacterial carbon fixation machinery. Science 327, 1258–1261.

Schindelin J, Arganda-Carreras I, Frise E, Kaynig V, Longair M, Pietzsch T, Preibisch S, Rueden C, Saalfeld S, Schmid B, et al. (2012). Fiji: an open-source platform for biological-image analysis. Nat Methods 9, 676–682.

Shaner NC, Lambert GG, Chammas A, Ni Y, Cranfill PJ, Baird MA, Sell BR, Allen JR, Day RN, Israelsson M, et al. (2013). A bright monomeric green fluorescent protein derived from Branchiostoma lanceolatum. Nat Methods 10, 407–409.

Tinevez JY, Perry N, Schindelin J, Hoopes GM, Reynolds GD, Laplantine E, Bednarek SY, Shorte SL, Eliceiri KW (2017). TrackMate: an open and extensible platform for single-particle tracking. Methods 115, 80–90.

Woodger FJ, Badger MR, Price GD (2005). Sensing of inorganic carbon limitation in Synechococcus PCC7942 is correlated with the size of the internal inorganic carbon pool and involves oxygen. Plant Physiol 139, 1959–1969.